



# Direct selective laser sintering of high-entropy carbide ceramics

Xiang Zhang<sup>1</sup>, Nan Li<sup>2</sup>, Xin Chen<sup>1</sup>, Mark Stroup<sup>1</sup>, Yongfeng Lu<sup>2</sup>, Bai Cui<sup>1,3,a)</sup> 

<sup>1</sup>Department of Mechanical & Materials Engineering, University of Nebraska–Lincoln, Lincoln, NE 68588, USA

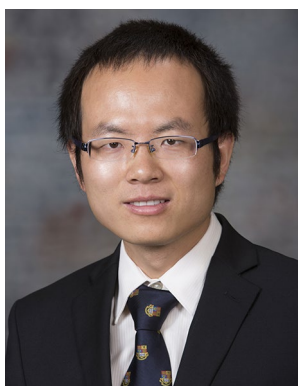
<sup>2</sup>Department of Electrical and Computer Engineering, University of Nebraska–Lincoln, Lincoln, NE 68588, USA

<sup>3</sup>Nebraska Center for Materials and Nanoscience, University of Nebraska–Lincoln, Lincoln, NE 68588, USA

<sup>a)</sup>Address all correspondence to this author. e-mail: bcui3@unl.edu

Received: 11 June 2022; accepted: 30 September 2022; published online: 25 October 2022

The direct selective laser sintering (SLS) process was successfully demonstrated for additive manufacturing of high-entropy carbide ceramics (HECC), in which a Yb fiber laser was employed for ultrafast (in seconds) reactive sintering of HECC specimens from a powder mixture of constitute monocarbides. A single-phase non-equiatomic HECC was successfully formed in the 4-HECC specimen with a uniform distribution of Zr, Nb, Hf, Ta, and C. In contrast, a three-layer microstructure was formed in the 5-HECC specimen with five metal elements (Zr, Nb, Hf, Ta and Ti), consisting of a TiC-rich top layer, a Zr–Hf–C enriched intermediate layer, and a non-equiatomic Zr–Ta–Nb–Hf–C HECC layer. Vickers hardness of 4- and 5-HECC specimens were 22.2 and 21.8 GPa, respectively, on the surface. These findings have important implications on the fundamental mechanisms governing interactions between laser and monocarbide powders to form a solid solution of HECCs during SLS.



Bai Cui

Bai Cui is the College of Engineering R. Vernon McBroom Associate Professor in the Department of Mechanical and Materials Engineering at the University of Nebraska–Lincoln (UNL), USA. He received his Bachelor's and Master's degrees in Materials Engineering from Tsinghua University in Beijing, and was awarded his Ph.D. in Materials Science from Imperial College London. He then served as a postdoctoral associate at the University of Illinois at Urbana-Champaign. Dr. Cui now leads the Materials for Extreme Environments (ME<sup>2</sup>) Lab at UNL, which develops advanced materials that can withstand extreme environments, such as high temperatures, irradiation, and corrosive gases or liquids, in next-generation energy systems. He has published over 80 journal papers. Dr. Cui has been recognized with the Global Star Award from Engineering Ceramics Division, American Ceramic Society (2022), the Faculty Research & Creative Activity Award from UNL College of Engineering (2021), and the Richard Brook Prize for Best Ph.D. in Ceramics in the UK (2012). He currently serves as a Senior Editor of Journal of Laser Applications, and the Chair of the Programming Committee, Manufacturing

Division of the American Ceramic Society. He was Chair of the Corrosion and Environmental Effects Committee in the Minerals, Metals & Materials Society (2019–20). Bai's research areas cover advanced metal and ceramic materials for extreme environments, laser additive manufacturing, and laser shock peening.

## Introduction

In recent years, the entropy engineering concept has been extended from metal alloys to ceramic materials to introduce promising opportunities for discovering novel structural and functional materials. High-entropy ceramics (HECs) contain at

least four metallic cation elements in an equal or near-equal atomic ratio in the cation positions, while a nonmetal element of C, B, N, or O occupies the anion positions [1–3]. Specifically, high-entropy carbides and borides bring new opportunities to expand the compositional space of ultra-high temperature

ceramics (UHTCs) with tailored physical and chemical properties within a single-phase solid solution [4–7].

High-entropy carbide ceramics (HECC) have a rock-salt cubic structure (space group Fm-3m), which exhibits the same crystal structure of the transition metal monocarbides. HECCs such as  $(\text{Hf}_{0.2}\text{Zr}_{0.2}\text{Ta}_{0.2}\text{Nb}_{0.2}\text{Ti}_{0.2})\text{C}$  were first reported by our group [8] and Castle et al. [9] in 2018, which were synthesized using spark plasma sintering (SPS) from monocarbide powders in equimolar concentrations. Since then, many unique physical properties have been reported in the literature such as higher hardness and high-temperature strength [10], lower thermal conductivity [8, 11], and improved irradiation resistance than the constitute monocarbides [12, 13]. The promising properties of HECCs have been attributed to the atomic-level disorder, compositional complexity, lattice distortion, etc., although the fundamental mechanisms governing the microstructure-property relationship remain to be elucidated [14]. These features enable HECCs as promising candidate materials for extreme environments, such as leading edges of hypersonic vehicles and carbide fuels or fuel claddings in fast reactors.

The most common manufacturing process of HECCs is the reactive sintering of a powder mixture of constitute monocarbides [8, 15], or metallic elements and carbon [16, 17], or metal oxides and carbon powders [18, 19]. Reactive sintering of HECCs has been successfully conducted by pressure-assisted processes including SPS and hot pressing, which require a high temperature from 1800 to 2300 °C and a pressure from tens of MPa to several GPa [20, 21]. Due to the high melting temperatures (>3000°C) and low diffusion coefficients resulted from the strong metal–carbon bonding of transition metal carbides, high temperature and pressure conditions are usually necessary to activate solid-state sintering via grain boundary and surface diffusion processes [22–24].

In recent years, additive manufacturing (AM, i.e., 3D printing) of ceramic materials has been explored to find out novel fabrication methods with a high cost efficiency [25, 26] and material utilization [27], which possess the ability to fabricate ceramic components with complex structures that are difficult to be produced by traditional methods [28]. The most popular AM techniques of ceramics, such as stereolithography, binder jetting, and inkjet printing, are “indirect” AM processes that apply polymer resins, binders, or inks into green bodies of ceramic powders to assist the shaping of 3D objects with a high precision [26, 29]. The post-heat treatments such as de-binding after AM are necessary to remove these polymers, which may induce significant porosity and cracks [26, 30, 31]. In many cases, a good microstructure can only be obtained after high-temperature sintering or hot isostatic pressing. [32–35]

Selective laser sintering (SLS) is a powder bed fusion 3D printing technology, which uses a continuous-wave (CW) laser beam to sinter the powders selectively and additively to build 3-D objects. The SLS processes can also be classified as “indirect” and “direct” SLS process [36]. The direct SLS process sinters the ceramic powders directly without polymer binders or resins, which has the advantages of a short process time (a few seconds), precise control by lasers, no contamination, and no post-heat treatment. There has been very few previous research related to the direct SLS of transition metal carbides. Bacciochini et al. developed a surface densification process using a ytterbium-doped fiber laser with a wavelength of 1072 nm and an output power of 100 W, which formed a dense ZrC thin film on the surface of porous ZrC ceramics [19]. In 2021, our team successfully developed a direct SLS process that used a CO<sub>2</sub> laser beam to directly sinter BaTiO<sub>3</sub> powders (binder-free) to enable rapid densification of a layer of over 500 μm with nearly 100% relative density [37].

This manuscript reported the feasibility of using direct SLS technique for AM of HECCs for the first time. HECCs were used as a model material to study the microstructural evolution of ceramic materials with complex compositions during SLS. In this study, the direct SLS process is a reactive sintering process to form HECC specimens from a powder mixture of constitute monocarbides. The phase formation and microstructural changes were revealed by electron microscopy characterizations to understand the fundamental mechanisms of laser-material interactions during the direct SLS. Hardness tests were conducted to evaluate the mechanical performance of the direct SLSed HECC specimens.

## Results and discussions

Two equimolar compositions of monocarbide powder mixtures were processed by high-energy ball milling process to prepare precursor powders of 4- and 5-HECC, respectively. The phase analysis of these precursor powders showed that the solid solution of high-entropy phase was not formed yet. XRD of precursor powders of the 4- and 5-HECC and five monocarbide powders are shown in Fig. 1(a). Because the lattice parameter difference between ZrC and HfC is only 0.60% (Table 1), their XRD peak positions are close to each other and may have merged in the precursor powders of 4- and 5-HECC. Similarly, due to the lattice parameter difference of only 0.53% between NbC and TaC, their XRD peak positions may have also merged. Secondary electron images of the precursor powders of the 4- and 5-HECCs are shown in Fig. 1(b) and (c), respectively. EDS mapping suggested that each constitute monocarbide remained in an isolated distribution. The average particle size of the precursor powders of 4-HECC reduced to 3.1 μm with an irregular

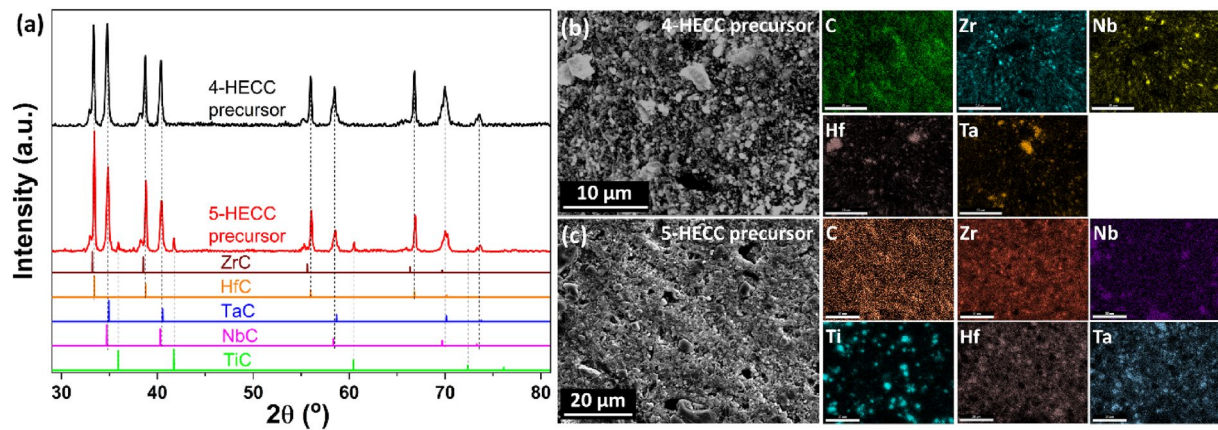


**Figure 1:** (a) XRD patterns of the ball-milled 4- and 5-HECC precursor powders, compared with the monocarbides ZrC, HfC, TaC, NbC, and TiC. Typical SEM images of (b) 4-HECC precursor powders, combined with EDS mapping of C, Zr, Nb, Hf, and Ta; and (c) 5-HECC precursor powders, combined with EDS mapping of C, Zr, Nb, Ti, Hf, and Ta.

**TABLE 1:** Crystallographic and physical data of the monocarbides and 4-HECC.

Component	Space group	Lattice parameter a (Å)	Melting temperature (°C) [9]	ICDD No.
ZrC	Fm-3m	4.669	3427	73-0477
HfC	Fm-3m	4.641	3959	73-0475
NbC	Fm-3m	4.470	3600	38-1364
TaC	Fm-3m	4.446	3768	77-0205
TiC	Fm-3m	4.328	3027	71-0298
4-HECC	Fm-3m	4.564	-	-

shape after ball milling, although some TaC and HfC powders may keep a coarser powder size of about 5.0 μm [Fig. 1(b)]. Likewise, the average powder size of the precursor powders of the 5-HECC decreased to 2.9 μm after ball milling.

During the direct SLS process (Fig. 8), a high-power (300–600 W) Yb fiber laser beam irradiated the loose precursor powders, during which the optical energy from the laser beam was transferred to the powders through the near-field photothermal effects to induce a rapid local temperature rise. Due to 50% overlapping ratio, most areas were scanned twice by the laser beam. Due to the moderate laser scanning speed ( $2.2 \times 10^{-4}$  m/s), the interaction time between the laser beam and powders was about 0.95 s at a laser spot. Although the laser beam diameter was set as 1 mm, the actual interaction area appeared to be higher as the laser beam can deposit energy into the neighbor area. The heat conduction can be extended to a significant depth from the surface due to the thermal conductivity of these monocarbides (6–34 W/m·K) [8] and cause sintering of the precursor powders. The laser power was found to be a key parameter for SLS of the HECCs. Almost complete densification was achieved by 600 W, while the specimen scanned by

laser powers of 300 and 450 W often broke into pieces. Thus, the SLSed 4- and 5-HECC specimens by 600 W were further analyzed by electron microscopy and mechanical tests.

Figure 2(a) to (c) show the surface morphology of the SLSed 4-HECC specimen. The ridge in the middle of Fig. 2(a) and (b) was the boundary between two adjacent laser scans. The whole surface was covered by isolated crystals with particle sizes of 1–5 μm, which were characterized as oxide particles of all four metal elements by EDS analysis [Fig. 2(d)]. These oxides may be formed from both the surface oxidation of monocarbide powder compact during the SLS process and the thin oxide layers in the commercial monocarbide powders. Based on the SEM images, the SLSed 4-HECC surface was fully densified with a relative density of >99% without noticeable voids or cracks. The average grain size was 13.56 μm, four times higher than the average particle size of the precursor powders (3.1 μm), indicating grain growth occurred during SLS. All four metal elements exhibited a uniform distribution on the surface without element segregation at grain boundaries according to the EDS mapping analysis.

Cross-section TEM lamellae were extracted from the SLSed 4-HECC specimen, which showed the near-surface microstructures from the surface to a depth of around 4 μm. HAADF image and EDS mapping analysis of the 4-HECC specimen revealed a uniform distribution of all four metal elements (Zr, Nb, Hf and Ta) and carbon [Fig. 3(a)]. The concentrations of four metal elements are: 16.3–18.5 at.%Zr, 28.3–29.4 at.%Ta, 12.5–16.6 at.%Nb, and 36.6–39.7 at.%Hf. The atomic percentage of carbon (C) is not counted into the quantitative results because the EDS analysis is not accurate for low-Z elements. Oxygen (O) was not detected by EDS, indicating that that oxidation only occurred on the top surface of specimens with Ar gas shielding. It is noted that the Nb concentration in the 4-HECC specimen is lower than other elements. The melting temperature of the

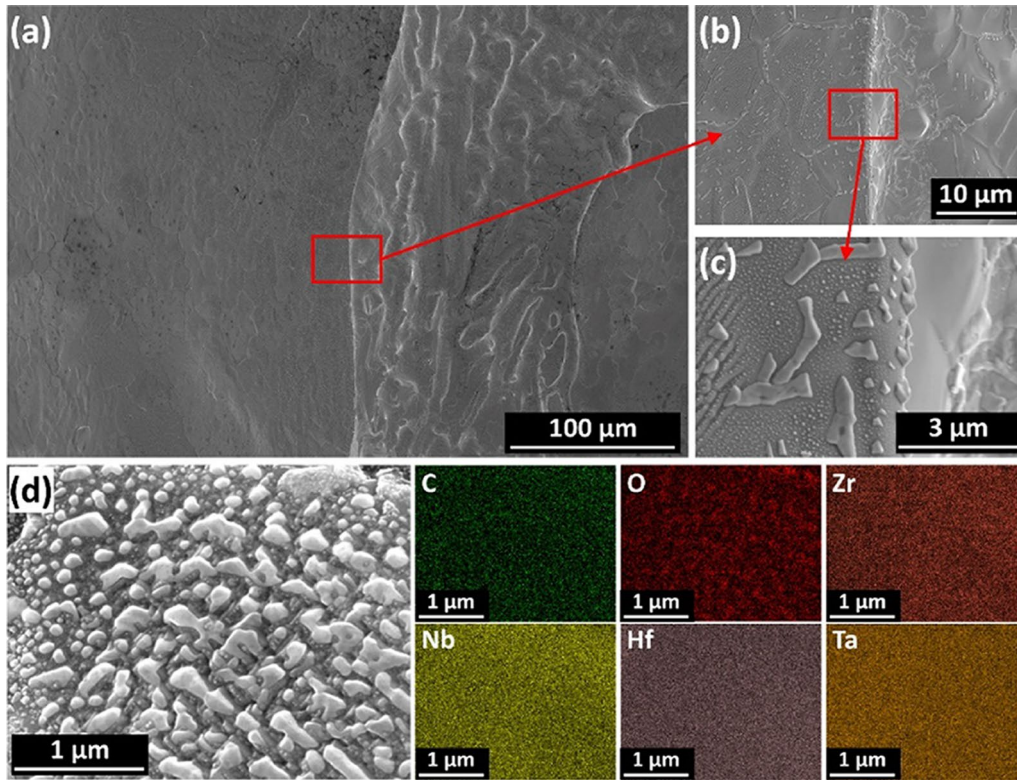


**Figure 2:** Typical surface morphologies (a–d) of the SLsed 4-HECC specimen along with EDS maps of C, O, Zr, Nb, Hf, and Ta. The laser power was 600 W.

oxides are:  $\text{Nb}_2\text{O}_5$  (1479 ~ 1595 °C) <  $\text{Ta}_2\text{O}_5$  (1872 °C) <  $\text{ZrO}_2$  (2794 °C) <  $\text{HfO}_2$  (2850 °C [38–41]). Among these oxides, niobium oxides seem to be most volatile. For example, Kofstad et al. determined that the evaporation rate of  $\text{Nb}_2\text{O}_5$  in vacuum ( $\sim 2 \times 10^{-5}$  Torr) is above  $0.04 \text{ mg}\cdot\text{cm}^{-2}\cdot\text{min}^{-1}$  at 1650 °C [42]. Semenov and Lopatin reported that the pressure of  $\text{NbO}_2$  gas at 2200 K in the thermodynamic equilibrium of vapor-condensed  $\text{Nb}_2\text{O}_5$  phase is 1.86 Pa, which is 8 times higher than the pressure of  $\text{TiO}_2$  gas (0.22 Pa) in  $\text{TiO}_2$  [43]. Thus, Nb loss in the 4-HECC specimen may be explained by the oxidation of NbC to  $\text{Nb}_2\text{O}_5$ , which melt at relatively low temperatures (1479 ~ 1595 °C) and then rapidly evaporate.

Further characterizations by diffraction-contrast bright-field [Fig. 3(b)] and high-resolution TEM (HRTEM)[Fig. 3(c)] images suggested that no noticeable defects, such as voids or dislocations, were presented in the HECC-4 specimen. The grain boundary in Fig. 3(b) is a random high-angle incoherent boundary. SAED analysis confirmed that SLsed 4-HECC has the rock-salt crystal structure (space group: Fm-3 m), which is the same for all constitute monocarbides. Figure 3(d) shows the high-resolution TEM (HRTEM) image of the left grain in Fig. 3(b), in which the (2 0 0) plane spacing was resolved as 2.282 Å. The lattice parameter of HECC-4 was calculated as 4.564 Å, close to the average lattice parameter (4.556 Å) of the four monocarbides ( $a_{\text{TaC}} < a_{\text{NbC}} < a_{4\text{-HECC}} < a_{\text{HfC}} < a_{\text{ZrC}}$ ) (Table 1). The combination of

SAED, EDS, and HRTEM characterizations suggest that a single-phase solid solution of non-equiatomic HECC was successfully formed in 4-HECC specimen by the novel SLS process.

Compared to 4-HECC specimens containing four metal elements of Zr, Ta, Nb and Hf, the fifth metal element Ti was added into the composition of 5-HECC specimens. Figure 4(a) shows the surface morphology of the 5-HECC specimen densified by a laser power of 600 W, in which the density was measured by ImageJ as > 99%. The average grain size was 36.1 μm, 10 times higher than the ball-milled precursor powder (2.9 μm). The surface of HECC-5 is more flat than the that of the 4-HECC with the absence of oxide crystals. However, the laser-scan-induced ripples and bulgy grain boundaries can be observed [Fig. 4(b) and (c)]. EDS mapping analysis indicated that Zr, Ta, Nb and Hf were distributed uniformly, while a slight enrichment of Ti may occur in the bulgy grain boundaries. The concentrations of five metal elements are: 9 ~ 14 at.%Zr, 4 ~ 7 at.%Ta, 7 ~ 10 at.%Nb, 12 ~ 14 at.%Hf, and 14 ~ 23 at.%Ti. This EDS analysis result includes all metal elements and carbon.

Figures 5(a) and (b) show the cross-sectional STEM HAADF images of the near-surface region of the SLsed 5-HECC specimen. EDS mapping [Fig. 5(a)] and line-scanning [Fig. 5(c)] analysis suggested that a three-layer microstructure may be formed. The top layer (200–300 nm thick) was enriched with Ti (39.4 ~ 88.2 at.%) and low concentrations of Zr (3.2 ~ 24.1 at.%),

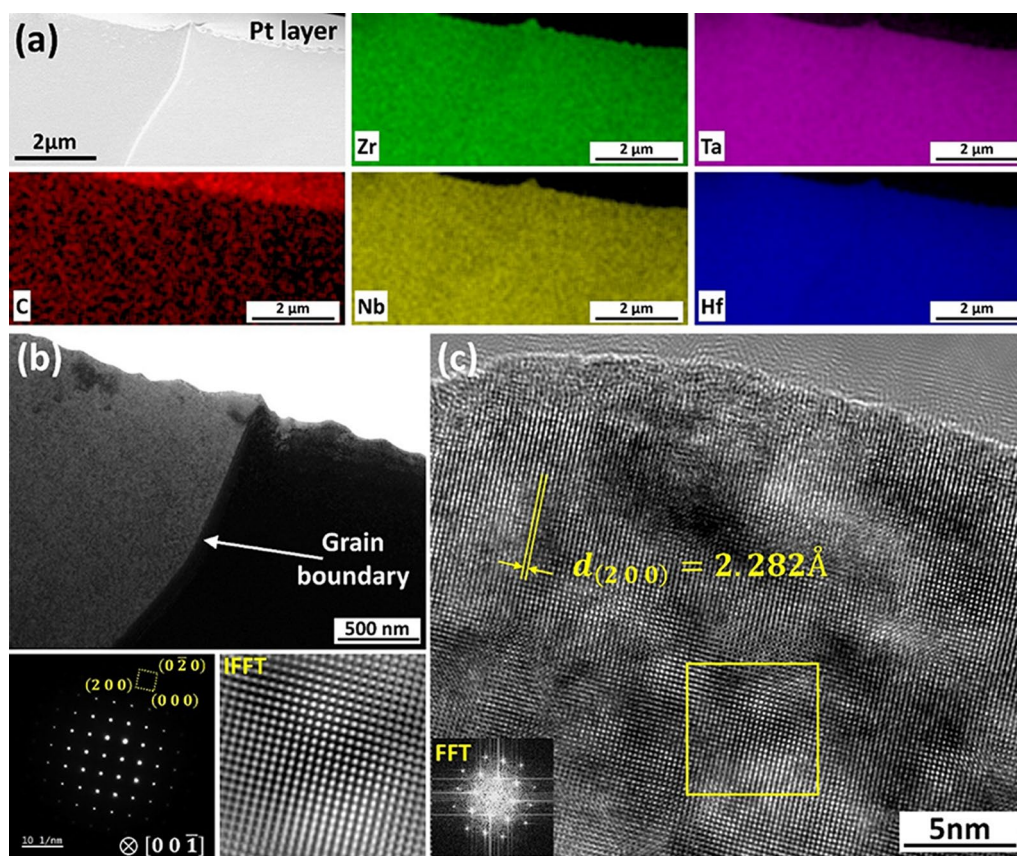


**Figure 3:** (a) Cross-section STEM high-angle annular dark field (HAADF) image of SLsed 4-HECC specimen along with EDS maps showing homogeneous elemental distributions of all metal elements and carbon. (b) Bright-field image of the near-surface region. The SAED pattern and (c) HRTEM images show the left grain in b). The fast Fourier transform (FFT) and inverse fast Fourier transform (IFFT) show the details in the yellow frame in (c).

Ta (3.3 ~ 8.5 at.%), Nb (0.1 ~ 5.1 at.%), and Hf (5.2 ~ 22.9 at.%). Underneath that, an intermediate layer (around 1  $\mu\text{m}$  thick) was enriched with Zr (24.1 ~ 24.6 at.%) and Hf (22.9 ~ 44.1 at.%), but lower concentrations of Ti (0.9 ~ 39.4 at.%), Ta (8.5 ~ 16.5 at.%), and Nb (5.1 ~ 13.9 at.%). The majority of the HECC-5 specimen (~ 7  $\mu\text{m}$  thick) is a non-equiatomic Zr-Ta-Nb-Hf-C HECC layer consisting of Zr (10.0 ~ 24.6 at.%), Ta (16.5 ~ 39.1 at.%), Nb (9.7 ~ 13.9 at.%), and Hf (40.8 ~ 44.1 at.%), which was depleted with Ti (< 1 at.%). These EDS analysis results include all metal elements and carbon.

Typical nano-beam electron diffraction patterns (i, ii, and iii in Fig. 5b) were taken from each layer to determine the lattice parameters. The three layers shared the same rock-salt crystal structure and orientation. Since the top layer was very thin (200–300 nm), the nano-beam diffraction i consisted of the overlapping patterns of the top layer (indicated by yellow dotted lines) and intermediate layer (indicated by red dotted lines), which was the same with the nano-beam diffraction from ii). The lattice parameter of the top layer was calculated as  $4.478 \pm 0.026 \text{ \AA}$ , which was 103.5% to that of TiC. The slight difference in lattice parameters may result from the solid-solution effect that other metal elements of Zr, Ta, Nb, and Hf

were dissolved into the TiC lattice. The lattice parameter of the intermediate layer was calculated as  $4.605 \pm 0.027 \text{ \AA}$ , which was 98.6 and 99.2% to that of ZrC and HfC, respectively. The lattice parameter of the HECC layer was calculated as  $4.540 \pm 0.026 \text{ \AA}$ , which was 99.5% to that of 4-HECC sample. It is noted that the lattice parameters of the top and intermediate layers showed a noticeable difference, while the lattice parameters of the intermediate and HECC layers was closer.

Diffraction-contrast bright-field TEM images (Fig. 6) were used to reveal the defects such as dislocations. The 4-HECC specimen was almost free of dislocations. Interestingly, a high density of dislocations formed at the interface between the intermediate and HECC layers in the 5-HECC specimen [Fig. 6(b)]. The Burgers vector ( $b$ ) of most dislocations was identified as  $1/2[101]$ , and their slip plane was parallel to the boundary. The origin of the dislocations may need further investigations. It is likely that these dislocations were generated by the thermal stress during the rapid cooling after SLS. Yan et al. measured the thermal expansion coefficient of  $(\text{Hf}_{0.2}\text{Zr}_{0.2}\text{Ta}_{0.2}\text{Nb}_{0.2}\text{Ti}_{0.2})\text{C}$  using a dilatometer, which was comparable to that of the five-constitute monocarbides (HfC, ZrC, TaC, NbC and TiC, in the range of  $6.3 \sim 7.0 \times 10^{-6} \text{ K}^{-1}$ ) [8]. Thus, thermal stress at the

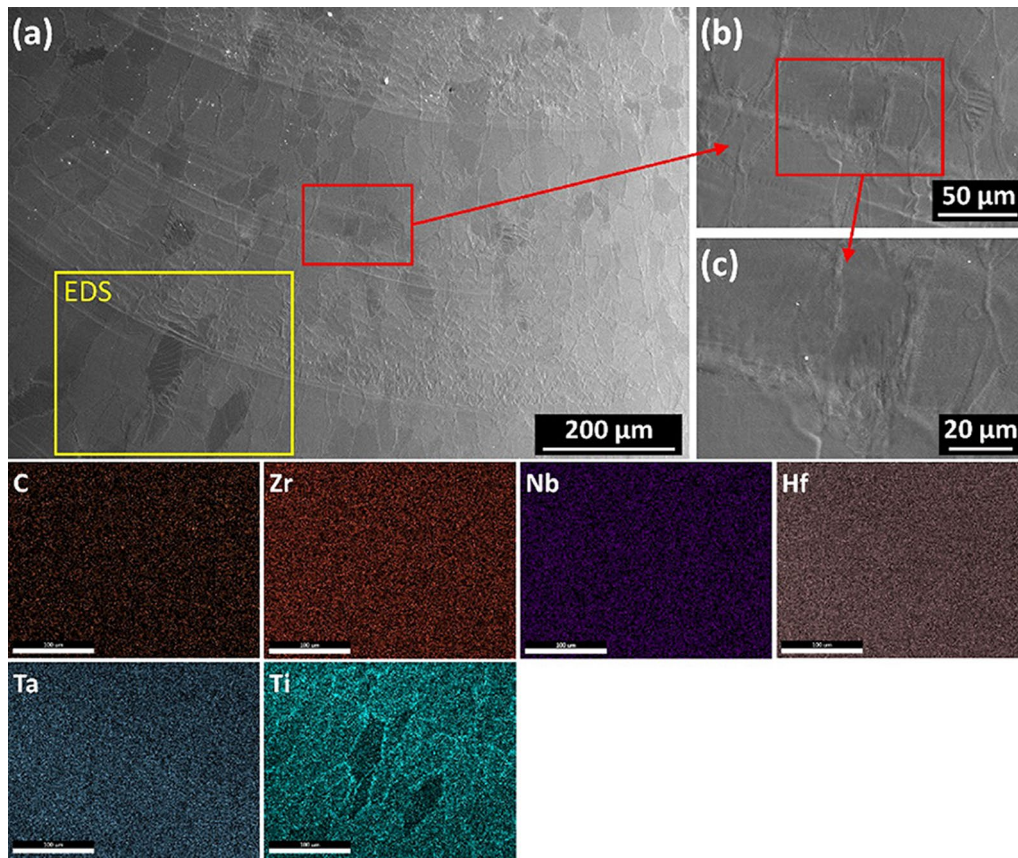


**Figure 4:** (a–c) Typical surface morphology of SLSed 5-HECC specimen, combined with EDS mapping of all elements. The laser power was 600 W.

interface may be negligible due to the small mismatch between thermal expansion coefficients of the intermediate (mainly Zr-Hf-C) and HECC (Zr-Ta-Nb-Hf-C) layers.

It is interesting to note that a single-phase solid solution of HECC can be formed in the 4-HECC specimens containing four metal elements of Zr, Ta, Nb and Hf, in contrast to the three-layer microstructure of the 5-HECC specimen when the fifth element of Ti is added. It is generally accepted that the metal self-diffusion is independent of carbon self-diffusion in the transition metal carbides, while the carbon self-diffusion coefficients measured are several orders of magnitude higher than the metal self-diffusion coefficients [44, 45]. The metal self-diffusion occurs via the formation of a nearest neighbor metal vacancy, which was dependent on both vacancy formation and migration energies. Among the five monocarbides (Table 1), TiC has the lowest melting temperature (3027°C) and smallest lattice parameter (4.328 Å). Based on the inter-diffusion analysis, Castle et al. suggested that the relative diffusion rates of metal elements in transitional metal carbides are Ta < Zr ~ Hf < Nb < Ti [9]. During the SLS process, a CW laser beam with a high-power of 600 W irradiated the loose precursor powders, which may cause at least the partial melting of TiC powder surfaces due to its lowest melting temperature, which may be segregated into the melt pool. The highest diffusion rate of Ti

may accelerate the segregation of TiC. During the rapid cooling after SLS, the TiC-rich top layer may be solidified from the melt pool, although this hypothesis needs to be verified via the accurate measurement of the local temperatures. The other four elements (Zr, Ta, Nb and Hf), due to higher melting temperatures and lower diffusion rates of the metal elements, were more likely to form a HECC phase in the solid state. Control experiments will be used in our future research to further investigate the segregation behavior during SLS of monocarbide powder mixtures at varied laser power, scan speed, and time. In addition, to elucidate the fundamental mechanisms of the layer formation, the in situ synchrotron X-ray diffraction experiments may be used to reveal the phase formation and transformation in the laser heated region (including the molten pool) during SLS of monocarbide powder mixtures [46, 47].

Vickers hardness tests (Fig. 7) show that 4- and 5-HECC samples have a hardness of 22.2 and 21.8 GPa, respectively, under an applied load of 3 N on the surface. The hardness of the 4-HECC sample decreased slightly along the depth direction, from 22.2 GPa on the surface to 18.8 GPa at a depth of 300 μm, and then stabilized at 15.0 GPa in deeper areas. For the 5-HECC sample, the Vickers hardness decreases significantly to 16.0 GPa at a depth of 200 μm. Nanoindentations of the 4- and 5-HECC samples will be performed to further characterize the local mechanical properties.

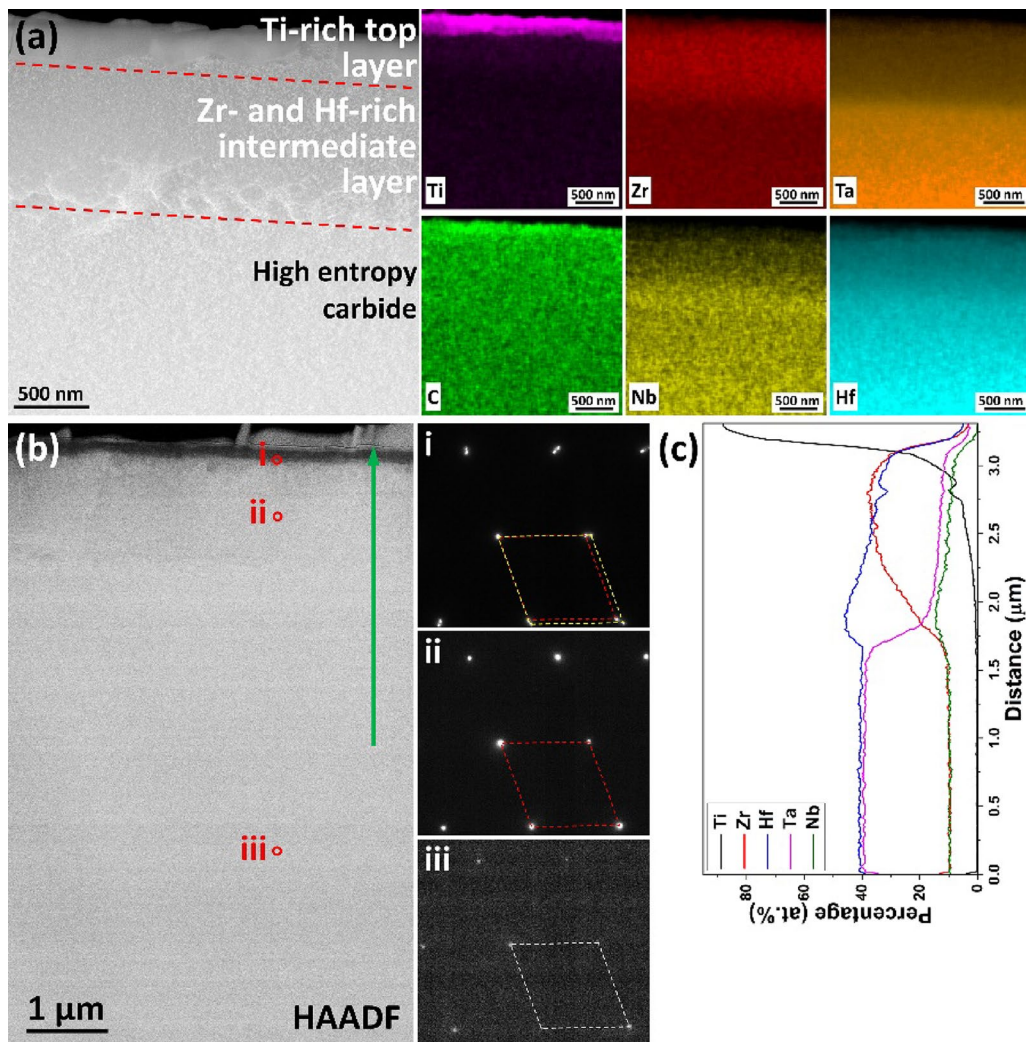


**Figure 5:** (a) Cross-section STEM HAADF images of 5-HECC specimen along with EDS maps of all elements. (b) The HAADF image with nano-beam diffraction patterns from areas i, ii, and iii. (c) EDS line-scan along the green arrow in (b), revealing the concentration change of metal elements on and below the surface.

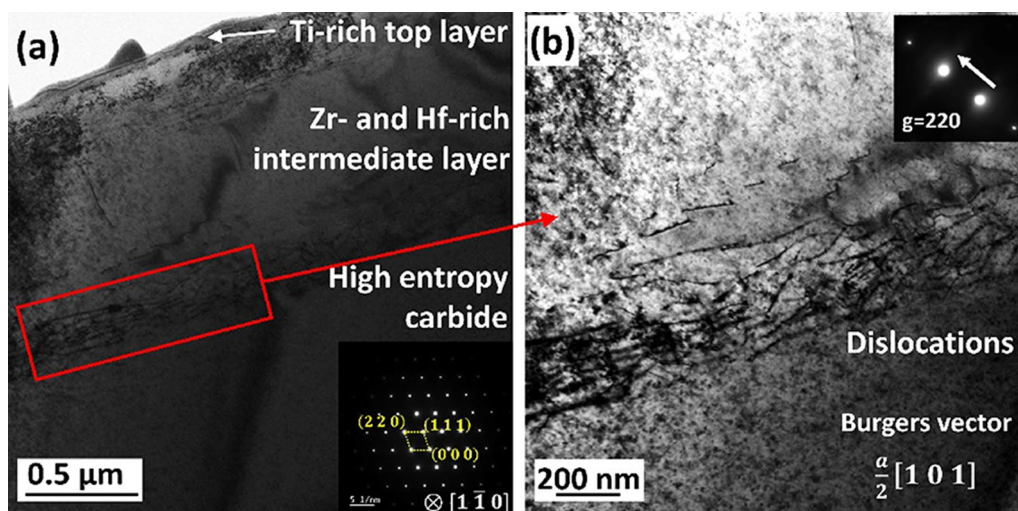


**Figure 6:** (a, b) Typical bright-field TEM images of the near-surface region of the 5-HECC specimen. The inserted SAED in a) presents the crystallographic feature of the HECC layer. Dislocation structures in b) were imaged using a two-beam diffraction-contrast condition with diffraction vector  $g = 2 2 0$ .

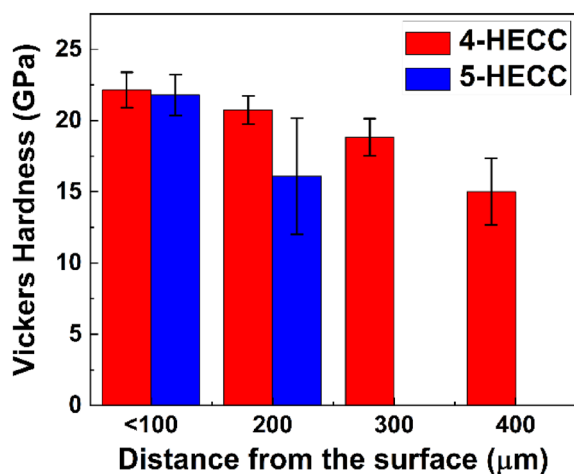


**Figure 7:** Vickers hardness along the cross sections of 4- and 5-HECC samples as functions of the distance from the sample surface. The applied load was 3 N.

## Conclusions

This manuscript reports the feasibility of applying the direct SLS technique for AM of HECCs for the first time. Ultrafast reactive sintering of HECC specimens was conducted using a powder mixture of constitute monocarbides. A relative density of >99% was achieved in seconds using a Yb fiber laser of 600 W. Two compositions, 4-HECC (Zr–Nb–Hf–Ta–C) and 5-HECC (Zr–Nb–Hf–Ta–Ti–C) showed different microstructures. A single-phase non-equiatom HECC was formed in the 4-HECC specimen with a uniform distribution of four metal elements and carbon. However, a three-layer microstructure was formed in the 5-HECC specimen, consisting of a TiC-rich top layer, a Zr–Hf–C enriched intermediate layer, and a non-equiatom Zr–Ta–Nb–Hf–C HECC layer. The formation mechanisms may be related to the interactions between laser and monocarbide powders to form a solid solution of HECCs during SLS. While the 4-HECC was almost free of dislocations, a high density of dislocations formed at the interface between the intermediate and HECC layers in the 5-HECC specimen. Vickers hardness of 4- and 5-HECC specimens were 22.2 and 21.8 GPa, respectively, under the applied load of 3 N on the surface.

## Materials and methods

Commercially available zirconium carbide (ZrC) powder (99.9%, 0.4–1.2 μm), hafnium carbide (HfC) (99.5%, <45 μm), tantalum carbide (TaC) (99.5%, <45 μm), niobium carbide (NbC) (99.0%, <45 μm), and titanium carbide (TiC) powders (99.5%, <45 μm) from Alfa Aesar were used in the experiments. Two compositions of monocarbide powder mixture were used

as the starting materials. The first composition has four monocarbides, i.e., HfC, NbC, TaC, and ZrC, which was used to fabricate 4-HECC specimens. The second one includes five monocarbides, i.e., HfC, NbC, TaC, TiC, and ZrC, which was used to prepare 5-HECC specimens. The crystallographic data and melting temperature of these monocarbides are listed in Table 1.

The starting monocarbide powders for 4- and 5-HECC were mixed at an equimolar ratio and then ball-milled with stainless-steel balls with a ball-to-powder ratio of 5:1. The ball-milling process was conducted using a planetary ball mill machine (Model Pulverisette 7, Fritsch GmbH) for 8 h at a speed of 350 rpm in an Argon gas environment to prevent oxidation, which was paused for 5 min after every 15 min of milling to avoid overheating. 10 g of powder mixtures were poured into a stainless-steel die with dimensions of 20 mm × 20 mm and then cold pressed at 125 MPa with a holding time of 15 s. The relative density of cold-pressed powder compact was about 33–36%. The powder compact with the stainless-steel die was transferred to a 3D hybrid vertical milling center system (Optomec LENS) that has a continuous-wave (CW) Yb-fiber laser source with a wavelength of 1064 nm and a maximum power of 1000 W [Fig. 8(a)]. Selective laser sintering (SLS) experiments [Fig. 8(b)] were conducted using a laser spot size of 1 mm, a scanning speed of  $2.2 \times 10^{-4}$  m/s, and laser powers of 300, 450, and 600 W, respectively, with argon (Ar) gas shielding. The scanning gap of the laser beam was 0.5 mm corresponding to an overlapping ratio of 50% [Fig. 8(c)].

Phases in the ball-milled powders and SLSed 4- and 5-HECC specimens were characterized by X-ray diffraction (XRD) using a X-ray diffractometer (SmartLab, Rigaku) with a Cu X-ray tube and operation conditions of 40 kV and 44 mA. XRD patterns were collected over the  $2\theta$  range of 28°–82° with a step size 0.02° and a dwell time of 0.06 s at each step. The morphology and microstructures were characterized by scanning electron microscopy (SEM) operated at the secondary electron imaging mode in an FIB/SEM dual-beam Nanolab instrument (Helios 660 NanoLab, FEI). Microstructures of the SLSed 4- and 5-HECC specimens were also characterized by cross-sectional transmission electron microscopy in a scanning transmission electron microscope (S/TEM, Tecnai Osiris, FEI) operated at 200 kV. TEM samples were extracted from the sample surfaces by a focused ion beam (FIB) using a FEI Helios 660 FIB and then thinned to electron transparency. The crystal structures were characterized by selective area electron diffraction (SAED) and nano-beam electron diffraction using a 1.0 nm diameter electron-beam probe. Dislocation structures were examined using two-beam diffraction-contrast bright-field imaging conditions. The Burgers vectors of dislocations were determined using the conventional  $g \cdot b$  invisibility condition. The elemental distributions of metals and carbon were analyzed by the energy-dispersive X-ray spectroscopy (EDS) using an EDS detector (Octane Super, EDAX) in the SEM instrument and a SiLi EDS



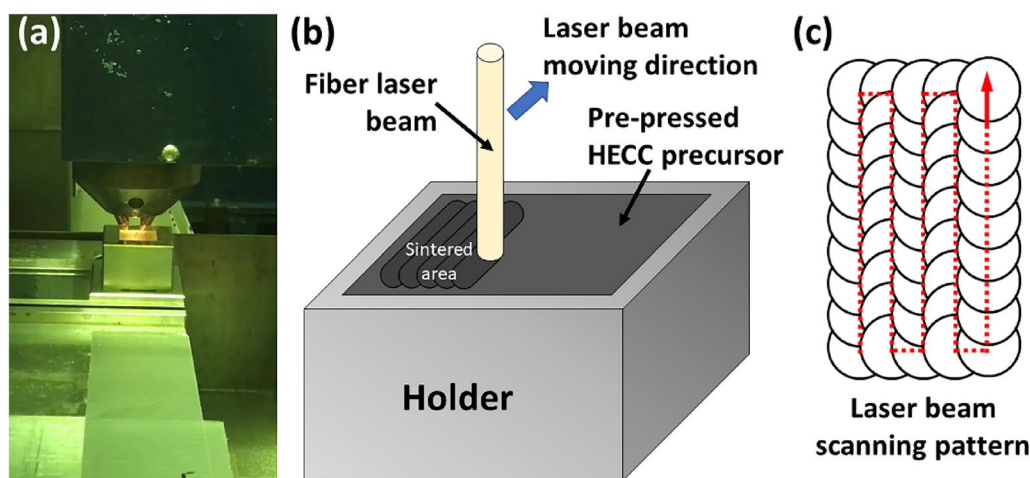


**Figure 8:** (a) Photo and (b) the schematic diagram of the experimental setup of SLS of HECC precursor powders by a Yb-fiber laser. (c) The laser scanning pattern during SLS.

detector (EDAMIV/DPP II, EDAX) in the S/TEM system. The intercept method was used to measure the grain and particle sizes from SEM images using ImageJ software. Vickers indentations were applied on the polished cross sections with an indentation load of 3 N and a dwell time of 10 s.

## Acknowledgments

B. Cui acknowledges the financial support from the Nuclear Regulatory Commission Faculty Development Grant (No. 31310018M0045) and University of Nebraska Research Council Interdisciplinary Grant. The research was performed in part in the Nebraska Nanoscale Facility: National Nanotechnology Coordinated Infrastructure and the Nebraska Center for Materials and Nanoscience (and/or NERCF), which are supported by the National Science Foundation under Award ECCS: 2025298, and the Nebraska Research Initiative.

## Data availability

The authors declare that all data supporting the findings of this study are available within the article.

## Declarations

**Conflict of interest** On behalf of all authors, the corresponding author states that there is no conflict of interest.

## Open Access

This article is licensed under a Creative Commons Attribution 4.0 International License, which permits use, sharing, adaptation, distribution and reproduction in any medium or format, as long as you give appropriate credit to the original author(s)

and the source, provide a link to the Creative Commons licence, and indicate if changes were made. The images or other third party material in this article are included in the article's Creative Commons licence, unless indicated otherwise in a credit line to the material. If material is not included in the article's Creative Commons licence and your intended use is not permitted by statutory regulation or exceeds the permitted use, you will need to obtain permission directly from the copyright holder. To view a copy of this licence, visit <http://creativecommons.org/licenses/by/4.0/>.

## References

1. H. Xiang, Y. Xing, F. Dai, H. Wang, L. Su, L. Miao, G. Zhang, Y. Wang, X. Qi, L. Yao, H. Wang, B. Zhao, J. Li, Y. Zhou, High-entropy ceramics: Present status, challenges, and a look forward. *J. Adv. Ceram.* **10**, 385–441 (2021)
2. W. Hong, F. Chen, Q. Shen, Y. Han, W.G. Fahrenholtz, L. Zhang, Microstructural evolution and mechanical properties of (Mg Co, Ni, Cu, Zn)O high-entropy ceramics. *J. Am. Ceram. Soc.* **102**, 2228–2237 (2018)
3. R.-Z. Zhang, M.J. Reece, Review of high entropy ceramics: design, synthesis, structure and properties. *J. Mater. Chem. A*. **7**, 22148–22162 (2019)
4. C. Niu, A.J. Zaddach, A.A. Oni, Spin-driven ordering of Cr in the equiatomic high entropy alloy NiFeCrCo. *Appl. Phys. Lett.* **106**, 161906 (2015)
5. D.B. Miracle, O.N. Senkov, A critical review of high entropy alloys and related concepts. *Acta Mater.* **122**, 448–511 (2017)
6. M. Qin, J. Gild, C. Hu, H. Wang, M.S. Bin Hoque, J.L. Braun, T.J. Harrington, P.E. Hopkins, K.S. Vecchio, J. Luo, Dual-phase high-entropy ultra-high temperature ceramics. *J. Eur. Ceram. Soc.* **40**, 5037–5050 (2020)

7. A.J. Wright, J. Luo, A step forward from high-entropy ceramics to compositionally complex ceramics: A new perspective. *J. Mater. Sci.* **55**, 9812–9827 (2020)
8. X. Yan, L. Constantin, Y. Lu, J.F. Silvain, M. Nastasi, B. Cui, (Hf<sub>0.2</sub>Zr<sub>0.2</sub>Ta<sub>0.2</sub>Nb<sub>0.2</sub>Ti<sub>0.2</sub>)C high-entropy ceramics with low thermal conductivity. *J. Am. Ceram. Soc.* **101**, 4486–4491 (2018)
9. E. Castle, T. Csanádi, S. Grasso, J. Dusza, M. Reece, Processing and properties of high-entropy ultra-high temperature carbides. *Sci. Rep.* **8**, 8609 (2018)
10. L. Feng, W.G. Fahrenholtz, D.W. Brenner, High-entropy ultra-high-temperature borides and carbides: a new class of materials for extreme environments. *Annu. Rev. Mater. Res.* **51**, 165–185 (2021)
11. E.C. Schwind, M.J. Reece, E. Castle, W.G. Fahrenholtz, G.E. Hilmas, C.C. Evan Schwind, Thermal and electrical properties of a high entropy carbide (Ta, Hf, Nb, Zr) at elevated temperatures. *J. Am. Ceram. Soc.* **105**, 4426–4434 (2022)
12. F. Wang, X. Yan, T. Wang, Y. Wu, L. Shao, M. Nastasi, Y. Lu, B. Cui, Irradiation damage in (Zr<sub>0.25</sub>Ta<sub>0.25</sub>Nb<sub>0.25</sub>Ti<sub>0.25</sub>)C high-entropy carbide ceramics. *Acta Mater.* **195**, 739–749 (2020)
13. Y. Zhu, J. Chai, Z. Wang, T. Shen, L. Niu, S. Li, P. Jin, H. Zhang, J. Li, M. Cui, Microstructural damage evolution of (WTiVNbTa)C<sub>5</sub> high-entropy carbide ceramics induced by self-ions irradiation. *J. Eur. Ceram. Soc.* **42**, 2567–2576 (2022)
14. C. Oses, C. Toher, S. Curtarolo, High-entropy ceramics. *Nat. Rev. Mater.* **5**, 295–309 (2020)
15. B. Ye, T. Wen, M.C. Nguyen, L. Hao, C.Z. Wang, Y. Chu, First-principles study, fabrication and characterization of (Zr<sub>0.25</sub>Nb<sub>0.25</sub>Ti<sub>0.25</sub>V<sub>0.25</sub>)C high-entropy ceramics. *Acta Mater.* **170**, 15–23 (2019)
16. D.O. Moskovskikh, S. Vorotilo, A.S. Sedegov, K.V. Kuskov, K.V. Bardasova, P.V. Kiryukhantsev-korneev, M. Zhukovskiy, A.S. Mukasyan, High-entropy (HfTaTiNbZr)C and (HfTaTiNbMo)C carbides fabricated through reactive high-energy ball milling and spark plasma sintering. *Ceram. Int.* **46**, 19008–19014 (2020)
17. D. Liu, A. Zhang, J. Jia, J. Meng, B. Su, Phase evolution and properties of (VNbTaMoW)C high entropy carbide prepared by reaction synthesis. *J. Eur. Ceram. Soc.* **40**, 2746–2751 (2020)
18. L. Feng, W.G. Fahrenholtz, G.E. Hilmas, Low-temperature sintering of single-phase, high-entropy carbide ceramics. *J. Am. Ceram. Soc.* **102**, 7217–7224 (2019)
19. X.-F. Wei, J.-X. Liu, F. Li, Y. Qin, Y.-C. Liang, G.-J. Zhang, High entropy carbide ceramics from different starting materials. *J. Eur. Ceram. Soc.* **39**, 2989–2994 (2019)
20. D. Demirskiy, H. Borodianska, T.S. Suzuki, Y. Sakka, K. Yoshimi, O. Vasylykiv, High-temperature flexural strength performance of ternary high-entropy carbide consolidated via spark plasma sintering of TaC, ZrC and NbC. *Scr. Mater.* **164**, 12–16 (2019)
21. R. Chang, C.G. Rhodes, High-pressure hot-pressing of uranium carbide powders and mechanism of sintering of refractory bodies. *J. Am. Ceram. Soc.* **45**, 379–382 (1962)
22. Y.U. Wang, Computer modeling and simulation of solid-state sintering: A phase field approach. *Acta Mater.* **54**, 953–961 (2006)
23. V. Tikare, M. Braginsky, E.A. Olevsky, Numerical simulation of solid-state sintering: I, sintering of three particles. *J. Am. Ceram. Soc.* **86**, 49–53 (2003)
24. J. Shi, Y. Deguchi, Y. Sakabe, Relation between grain growth, densification and surface diffusion in solid state sintering—a direct observation. *J. Mater. Sci.* **40**, 5711–5719 (2005)
25. S.A.M. Tofail, E.P. Koumoulos, A. Bandyopadhyay, S. Bose, L. O’Donoghue, C. Charitidis, Additive manufacturing: Scientific and technological challenges, market uptake and opportunities. *Mater. Today.* **21**, 22–37 (2018)
26. Y. Lakhdar, C. Tuck, J. Binner, A. Terry, R. Goodridge, Additive manufacturing of advanced ceramic materials. *Prog. Mater. Sci.* **116**, 100736 (2021)
27. M. Brandt, *Laser additive manufacturing: materials, design, technologies, and applications*, Woodhead Publishing (2016)
28. T. Ibn-Mohammed, C.A. Randall, K.B. Mustapha, J. Guo, J. Walker, S. Berbano, S.C.L. Koh, D. Wang, D.C. Sinclair, I.M. Reaney, Decarbonising ceramic manufacturing: A techno-economic analysis of energy efficient sintering technologies in the functional materials sector. *J. Eur. Ceram. Soc.* **39**, 5213–5235 (2019)
29. J.-C. Wang, H. Dommati, S.-J. Hsieh, Review of additive manufacturing methods for high-performance ceramic materials. *Int. J. Adv. Manuf. Technol.* **103**, 2627–2647 (2019)
30. K. Liu, J. Xu, X. Gu, C. Liu, H. Sun, H. Sun, S. Liu, Effects of raw material ratio and post-treatment on properties of soda lime glass-ceramics fabricated by selective laser sintering. *Ceram. Int.* **46**, 20633–20639 (2020)
31. T.D. Ngo, A. Kashani, G. Imbalzano, K.T.Q. Nguyen, D. Hui, Additive manufacturing (3D printing): A review of materials, methods, applications and challenges. *Composite B* **143**, 172–196 (2018)
32. R. Singh, A. Gupta, O. Tripathi, S. Srivastava, B. Singh, A. Awasthi, S.K. Rajput, P. Sonia, P. Singhal, K.K. Saxena, Powder bed fusion process in additive manufacturing: An overview. *Mater. Today Proc.* **26**, 3058–3070 (2019)
33. A. Yegyan Kumar, Y. Bai, A. Eklund, C.B. Williams, The effects of hot isostatic pressing on parts fabricated by binder jetting additive manufacturing. *Addit. Manuf.* **24**, 115–124 (2018)
34. K. Liu, Y. Shi, W. He, C. Li, Q. Wei, J. Liu, Densification of alumina components via indirect selective laser sintering combined with isostatic pressing. *Int. J. Adv. Manuf. Technol.* **67**, 2511–2519 (2013)
35. A.-N. Chen, J.-M. Wu, K. Liu, J.-Y. Chen, H. Xiao, P. Chen, C.-H. Li, Y.-S. Shi, High-performance ceramic parts with complex shape prepared by selective laser sintering: a review. *Adv. Appl. Ceram.* **117**, 100–117 (2018)

36. X. Zhang, X. Wu, J. Shi, Additive manufacturing of zirconia ceramics : a state-of-the-art review. *Integr. Med. Res.* **9**, 9029–9048 (2020)
37. X. Zhang, F. Wang, Z. Wu, Y. Lu, X. Yan, M. Nastasi, Y. Chen, Y. Hao, X. Hong, B. Cui, Direct selective laser sintering of hexagonal barium titanate ceramics. *J. Am. Ceram. Soc.* **104**, 1271–1280 (2021)
38. N.F.H. Bright, J.F. Rowland, The binary system CaO-Nb<sub>2</sub>O<sub>5</sub>. *J. Am. Ceram. Soc.* **48**, 329–334 (1962)
39. A. Awasthi, M. Gaune-Escard, M. Gaune-Escard, The O-Ta (Oxygen-Tantalum) system. *J. Phase Equilibria.* (1996).
40. C. Wang, M. Zinkevich, F. Aldinger, On the thermodynamic modeling of the Zr-O system. *Calphad Comput. Coupling Phase Diagr. Thermochem.* **28**, 281–292 (2004)
41. J.P. Coutures, J. Coutures, The system HfO<sub>2</sub>-TiO<sub>2</sub>. *J. Am. Ceram. Soc.* **70**, 383–387 (1987)
42. P. Kofstad, S. Espevik, Low-pressure oxidation of niobium at 1200 degrees - 1700 degrees C. *J. Electrochem. Soc.* **112**, 153 (1965)
43. G.A. Semenov, S.I. Lopatin, A study of evaporation in the TiO<sub>2</sub>-Nb<sub>2</sub>O<sub>5</sub> oxide system by high-temperature mass-spectrometry. *Russ. J. Appl. Chem.* **74**, 901–906 (2001)
44. S. Sarian, Diffusion of <sup>44</sup>Ti in TiCx. *J. Appl. Phys.* **40**, 3515 (2003)
45. B.J. Demaske, A. Chernatynskiy, S.R. Phillpot, First-principles investigation of intrinsic defects and self-diffusion in ordered phases of V<sub>2</sub>C. *J. Phys. Condens. Matter.* **29**, 245403 (2017)
46. C. Zhao, K. Fezzaa, R.W. Cunningham, H. Wen, F. De Carlo, L. Chen, A.D. Rollett, T. Sun, Real-time monitoring of laser powder bed fusion process using high-speed X-ray imaging and diffraction. *Sci. Rep.* **7**, 1–11 (2017)
47. E. Uhlmann, E. Krohmer, F. Schmeiser, N. Schell, W. Reimers, A laser powder bed fusion system for in situ x-ray diffraction with high-energy synchrotron radiation. *Rev. Sci. Instrum.* **91**, 075104 (2020)

**Publisher's Note** Springer Nature remains neutral with regard to jurisdictional claims in published maps and institutional affiliations.